Optimal ligand discrimination by asymmetric dimerization and turnover of interferon receptors

Patrick Binder[a,b,c,1], Nikolas D. Schnellbächer[a,b,1], Thomas Höfer[b,c], Nils B. Becker[b,c,2], and Ulrich S. Schwarz[a,b,2]

[a]Institute for Theoretical Physics, Heidelberg University, 69120 Heidelberg, Germany; [b]BioQuant–Center for Quantitative Biology, Heidelberg University, 69120 Heidelberg, Germany; and [c]Theoretical Systems Biology, German Cancer Research Center, 69120 Heidelberg, Germany

Edited by Alan S. Perelson, Los Alamos National Laboratory, Los Alamos, NM, and accepted by Editorial Board Member Herbert Levine August 11, 2021 (received for review February 26, 2021)

In multicellular organisms, antiviral defense mechanisms evoke a reliable collective immune response despite the noisy nature of biochemical communication between tissue cells. A molecular hub of this response, the interferon I receptor (IFNAR), discriminates between ligand types by their affinity regardless of concentration. To understand how ligand type can be decoded robustly by a single receptor, we frame ligand discrimination as an information-theoretic problem and systematically compare the major classes of receptor architectures: allosteric, homodimerizing, and heterodimerizing. We demonstrate that asymmetric heterodimers achieve the best discrimination power over the entire physiological range of local ligand concentrations. This design enables sensing of ligand presence and type, and it buffers against moderate concentration fluctuations. In addition, receptor turnover, which drives the receptor system out of thermodynamic equilibrium, allows alignment of activation points for ligands of different affinities and thereby makes ligand discrimination practically independent of concentration. IFNAR exhibits this optimal architecture, and our findings thus suggest that this specialized receptor can robustly decode digital messages carried by its different ligands.

immune response | signal transduction | information theory | cell–cell communication | robust sensing

Tissue cells communicate through a wide variety of chemical signals including hormones, growth factors, and cytokines. To elicit a response, incoming signals must first cross the membrane of a receiving cell, typically activating a membrane receptor. This initial step in signal transduction is decisive because intracellular pathways may process, amplify, and integrate signals (1–3), but cannot recover information lost at the receptor stage (4–6). Membrane receptor systems often already integrate, filter, and shape signals, exploiting nonlinear activation (7) or temporal (8–10) and spatiotemporal activation dynamics (11, 12). This suggests that information processing at the membrane enables cells to transmit relevant signals but reject noise, establishing a robust communication channel. Understanding the information-theoretic properties of receptor systems (13–15) is instrumental for clarifying the biological function of signaling pathways.

Here, we consider the problem of ligand discrimination, where the relevant signal is the type of ligand present in the cellular environment, rather than its concentration. We focus on membrane receptors mediating cell-to-cell communication, motivated by the phenomenon of affinity sensing in the type I interferon (IFN) cytokine receptor system. Cells infected by virus can alert neighboring cells by secreting IFN, to which these respond by antiviral or antiproliferative behavior. In humans, 17 different type I IFN ligands are known (13 IFNα subtypes and IFNβ, ϵ, κ, and ω), which bind to a single dimeric receptor (IFNAR) with widely varying affinities (16–18). The evolutionary advantages of this diversity are not fully understood. It has been a puzzling finding that different IFN types elicit different cellular responses, effectively multiplexing (19) different signals through the shared pathway component IFNAR, in a way that is independent of concentration: IFNβ can inhibit cell proliferation while saturating concentrations of a lower-affinity IFN variant cannot (20). Several possible mechanisms for affinity sensing have been proposed, including effects of downstream gene expression feedback (16), bistability (21), corralling of receptors on the membrane (22), and the kinetics of dimer-receptor activation (23). A related and widely studied topic is foreign vs. self-peptide discrimination in adaptive immunity (24–28). It has been predicted theoretically and shown experimentally that signaling pathways operating by kinetic-proofreading schemes downstream of receptors can read out the dwell times of ligands to optimally separate multiple self and foreign antigens in heterogeneous environments (29–32).

Here, we ask what generic features enable a cytokine receptor system to discriminate between ligand types directly at the membrane, overcoming the challenges of a tissue environment where local ligand concentrations can vary over several orders of magnitude (33). To address the question quantitatively, we formulate the combined tasks of detecting the presence of ligands and discriminating between different ligands as an information-processing problem and compare the respective performance of the three most important membrane receptor architectures. We find that single-unit receptors, which transmit information across the membrane by an allosteric mechanism, cannot reliably discriminate ligand type. Receptors that transmit information by ligand-induced oligomerization, however, can enable ligand discrimination. While homodimerizing receptors resolve

Significance

Upon viral infection, cytokine signaling molecules coordinate the immune response, but their distributions are highly inhomogeneous due to localized production and degradation in the infected tissue. It is a long-standing question how cytokine receptors can nevertheless decode inflammatory signals reliably. Here, we formulate this question as an inference problem in information theory and show that the molecular architecture of a receptor system determines its ability to discriminate between ligand types. Our results suggest that the type I interferon cytokine receptors have evolved the optimal design to detect and separate the presence of different ligand types in a noisy environment.

Author contributions: T.H., N.B.B., and U.S.S. designed research; P.B., N.D.S., and N.B.B. performed research; and P.B., N.D.S., T.H., N.B.B., and U.S.S. wrote the paper.

The authors declare no competing interest.

This article is a PNAS Direct Submission. A.S.P. is a guest editor invited by the Editorial Board.

[1]P.B. and N.D.S. contributed equally to this work.

[2]To whom correspondence may be addressed. Email: schwarz@thphys.uni-heidelberg.de or nils.becker@dkfz-heidelberg.de.

This article contains supporting information online at https://www.pnas.org/lookup/suppl/doi:10.1073/pnas.2103939118/-/DCSupplemental.

Published September 10, 2021.

ligand presence and type only in well-controlled environments, heterodimerizing receptors discriminate ligands very robustly, through efficient buffering of concentration fluctuations. Finally, active turnover of receptors can improve performance further by independently setting activation point and level of the response curve. IFNAR combines all these features and therefore appears to have evolved an optimal solution for robust ligand discrimination at the cell membrane.

Results

Ligand Discrimination as an Information-Processing Task. Fig. 1*A* schematically depicts the situation of interest. Upon viral infection, single cells in the tissue produce cytokines that are subject to diffusion and degradation in the tissue. Receiving cells sense different cytokines through a shared receptor system and elicit an intracellular response in the form of phosphorylated readout molecules. For type I interferon, the receptor is IFNAR and the readout molecules are phosphorylated STAT (pSTAT) transcription factors. Adopting the perspective of information theory (34–36), we view ligand discrimination as an inference problem to be solved by the cell: *Given the number of intracellular readout molecules, determine if extracellular ligand is present and decide on its type.* To formalize this notion, we characterize the receptor input by a random variable x with values $\{\alpha, \beta, \varnothing\}$, corresponding to steady states with presence of ligand of type α, β or no ligand, respectively. In particular, the option $x = \varnothing$ allows us to address sensing ligand presence regardless of type. Discrimination of true signal from subthreshold or unspecific ligand is an essential requirement for any receptor system and hence is a constitutive feature of our theory. As receptor output, we take the fluctuating intracellular number n of activated readout molecules. The performance of a receptor system regarding this inference problem is measured in bits by the mutual information:

$$I = I[p(x,n)] = \left\langle \log_2 \frac{p(x,n)}{p(x)p(n)} \right\rangle = \left\langle \log_2 \frac{p(n|x)}{\sum_x p(n|x)p(x)} \right\rangle, \quad [1]$$

which is the average reduction in uncertainty about the input x when the output n is known. Angled brackets indicate averages over the joint distribution $p(x,n)$. By the data processing inequality (4), the information available after further processing downstream, for example by pSTAT dimers binding to distinct classes of regulatory sites on DNA (20), is bounded by Eq. **1**. Thus, I quantifies the ability of a cell with input–output relation $p(n|x)$ to adapt to the environment x characterized by $p(x)$. We call I the discrimination power of the system. I could be measured experimentally by targeted induction of ligand secretion from sparse producer cells followed by flow cytometry of tissue cells for phosphorylated readout molecules (32, 37).

In order to calculate the discrimination power I for different receptor architectures of interest, we track the flow of information by a sequence of probability distributions as shown in Fig. 1*B*. First, we decompose the input distribution as follows:

$$p(x) = \begin{cases} 1 - p_\pi & x = \varnothing \\ p_\pi p_\tau(x) & x \in \{\alpha, \beta\} \end{cases}, \quad [2]$$

which assigns probability p_π to ligand being present, and if so, $p_\tau(\alpha)$ to type α and $p_\tau(\beta) = 1 - p_\tau(\alpha)$ to type β. The discrimination power decomposes accordingly,

$$I = I_\pi + p_\pi I_\tau, \quad [3]$$

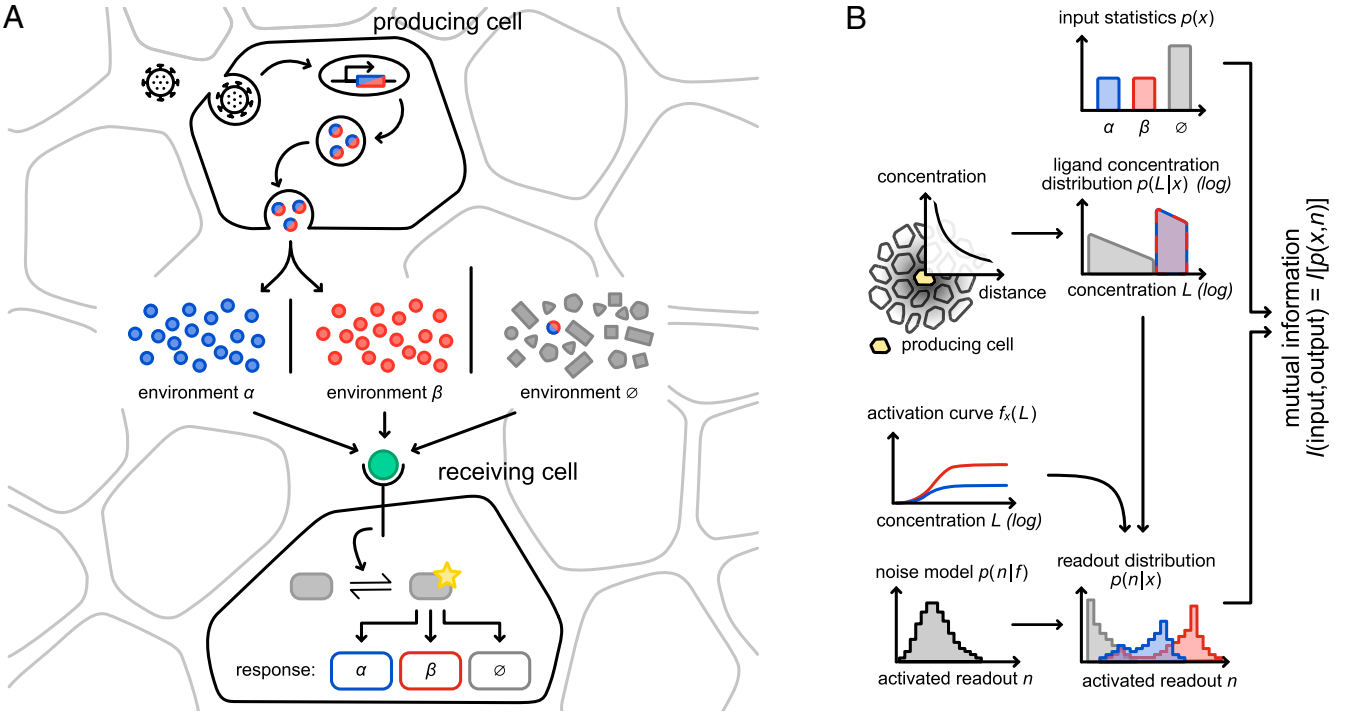

Fig. 1. Signal processing by membrane receptors. (*A*) From *Top* to *Bottom*: Viral infection leads to cytokine secretion by infected host cells. Extracellular environments with ligand α, β, or subthreshold ligand ($\varnothing$) are sensed by receptors at the membrane of receiving cells. Activated receptors phosphorylate readout molecules, which effect appropriate cellular responses. (*B*) Probability distributions involved in the signaling processing depicted in *A*: Probabilities of ligand environments; ligand concentration distribution for a given environment; average receptor activation depending on receptor architecture; distribution of activated readout molecules for given receptor activation; and finally, the distributions of activated readout molecules that determine how well the shared receptor can discriminate between different ligands. Overall system performance is quantified by mutual information I, which is measured in bits and in our context is interpreted as discrimination power.

where I_π is the information contained in n about ligand presence and I_τ, the information in n about ligand type (*SI Appendix*, section 1). As is biologically plausible, for good discrimination power a system needs to both detect ligand and distinguish the ligand types, a requirement that would not be captured by measuring performance as the concentration range over which activation levels are different, known as absolute discrimination window (27).

To proceed, we require a specific input distribution. As a parsimonious choice, we allow equal chances of ligand being absent or present, and of types α and β: $p_\pi = p_\tau(\alpha) = 1/2$ (Fig. 1*B*). Because I_π and I_τ reflect binary inputs, the total discrimination power is then limited to $I \leq 1.5$ bits. Alternative scenarios of rare inflammation ($p_\pi < 1/2$) and unequal ligand abundances ($p_\tau(\beta) < 1/2$) can also be treated (*Discussion*).

The input–output relation $p(n|x)$ decomposes according to the stages of information propagation in the system (Fig. 1*B*):

$$p(n|x) = \int p(n|L,x)p(L|x)\,dL. \qquad [4]$$

Here, $p(L|x)$ is the distribution of the ligand concentration L for given ligand type, discussed in the following subsection. The distribution $p(n|L,x)$ of activated readout molecules is a property of the receiving cell, determined by the activation curve and by molecular noise. The activation curve is the fraction $f_x(L)$ of activated receptors for given ligand type $x = \alpha, \beta$; it depends on the receptor architecture as discussed below. Activated receptors phosphorylate intracellular readout molecules at a rate proportional to $f = f_x(L)$, which entails molecular readout noise. We choose a simple Poisson form:

$$p(n|f) = e^{-\bar{n}f}(\bar{n}f)^n/n!, \qquad [5]$$

which is valid in a linear regime with weakly phosphorylated readout molecules; the readout number $\bar{n}$ is the mean number of phosphorylated readout molecules at full activation, which sets the level of intrinsic molecular noise in the receptor system (*SI Appendix*, section 1). Other sources of noise in a receptor system include cell-to-cell variability of receptor numbers and molecular noise in receptor activation. Here, we consider constitutively expressed receptors with unimodal distributions, which allows us to summarily treat additional noise sources by adjusting $\bar{n}$ (*Discussion*). From activation curve and noise model, we calculate the transfer functions by Eq. **5** as $p(n|L,x) = p(n|f_x(L))$ for each ligand, and finally, the non-Poissonian output distributions via Eq. **4**. From Eq. **1**, we then obtain the desired mutual information I as depicted in Fig. 1*B*.

Distributions of Local Cytokine Concentration. In a typical early-stage viral infection, a small percentage of infected cells produce and secrete inflammatory cytokines, which are consumed by a majority of receiving cells (Fig. 1*A*). Cytokine production, transport, and degradation result in a steady state where producer cells are surrounded by domains of elevated ligand concentration of size $\nu \simeq 100$ μm (38), termed cytokine niches (Fig. 1*B*) (37, 39). In the simplest model, cytokines spread diffusively and are degraded with a linear rate, so that the cytokine concentration decays exponentially with increasing distance to the producer. As a result, local cytokine concentrations L experienced by receiving cells vary widely, depending on the distance to producers and intervening degradation in the tissue. The stationary spatial ligand profiles uniquely determine the distribution $p(L|x)$ of concentrations experienced by a receiving cell sampled uniformly from the tissue (*SI Appendix*, section 2). In one spatial dimension, the exact result is the scale-free distribution:

$$p(L|x) = [\log(L_{\rm hi}/L_{\rm lo})]^{-1} L^{-1}. \qquad [6]$$

This expression remains a good approximation in two and three dimensions, and we note in passing that this result is also the scale-invariant noninformative prior (40) with L as scale parameter. The upper limit $L_{\rm hi}$ is attained in the immediate vicinity of producer cells; the lower limit $L_{\rm lo}$ is set by the average spacing 2σ of producers. In early inflammation, when signaling is crucial but producers are sparse, producer neighborhoods are much larger than cytokine niches ($\sigma > \nu$), so the fold-concentration range $L_{\rm hi}/L_{\rm lo} = \exp(\sigma/\nu)$ can become very large. We conclude that diffusion and degradation in a tissue generically lead to broad scale-free concentration distributions at receiving cells.

Based on these considerations, we model the ligand concentration distribution $p(L|x)$ in presence of either ligand by Eq. **6** with $L_{\rm lo} \equiv L_{\rm thr}$, where the lower concentration limit is the natural threshold concentration for detection of ligand by a receptor system (cf. Fig. 1*B*, red/blue). We set a fixed value $L_{\rm thr} = 10$ pM, which is comparable to the detection threshold found experimentally in the IFN system (41). We then vary $L_{\rm hi}$ over the range $10^2 L_{\rm thr} - 10^6 L_{\rm thr}$; this corresponds to an average spacing between producing cells of $2\sigma \simeq 9\nu - 28\nu$, respectively. These ranges reflect the fact that physiologically relevant cytokine concentration distributions span many orders of magnitude.

Absence of ligand ($x = \varnothing$) is represented by placing producer cells of both α and β outside the relevant tissue region, producing concentration distributions given by Eq. **6**, but this time limited to variable subthreshold ligand concentrations by setting $L_{\rm hi} \equiv L_{\rm thr}$ and $L_{\rm lo} \equiv 10^{-8} L_{\rm thr}$ (cf. Fig. 1*B*, gray). Nonspecific binding of other ligands is not represented explicitly but would result in a similar baseline of spurious low-level activation.

Receptor Architecture Shapes Response Curves. With the help of the information-theoretic framework introduced above, we now systematically compare the most important classes of cytokine receptor architectures. We first recall how receptor architecture determines the steady-state dose–response of receptor activation and begin with receptors that use allosteric transmission as shown in Fig. 2*A*. In allosteric transmission, a ligand-induced extracellular conformational change is propagated to a cytosolic effector domain, where it modifies enzymatic rates. The receptor functions as a single unit, whether it exists as a monomer [e.g.,

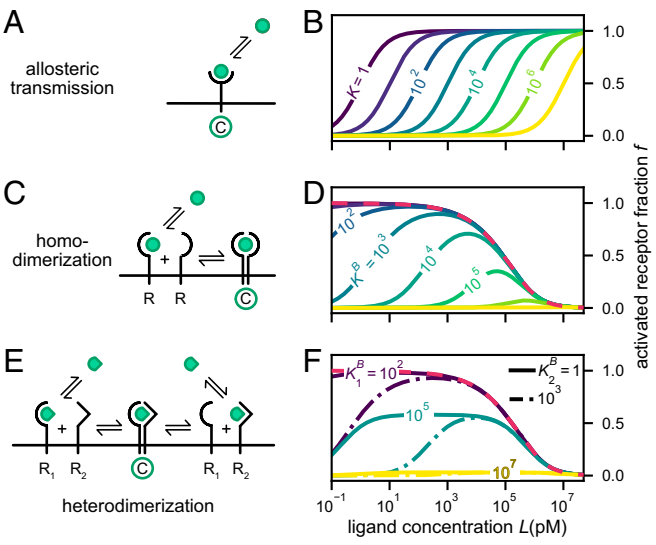

Fig. 2. Response repertoire of basic receptor architectures. (*A*) Allosteric receptors and (*B*) activation curves. (*C*) Homodimerizing receptors and (*D*) activation curves. (*E*) Heterodimerizing receptors and (*F*) activation curves. R, receptor chains; C, active receptor complex in *A*, *C*, and *E*. In *D* and *F*, limiting curves at high affinities are shown as dashed and total receptor density $2R_0 = 2\ \mu m^{-2}$. Dissociation constants K are in picomolar concentration.

the G-protein–coupled receptors β_2AR and CXCR1 (42)] or as a preformed oligomer [e.g., CXCR2 (42) and other chemokine receptors (43)]. In the simplest implementation, the receptor R is (in)active whenever ligand L is (un)bound, corresponding to the scheme $\mathrm{R}+\mathrm{L}\rightleftharpoons\mathrm{RL}$. With excess of free ligand, the equilibrium fraction f of active receptors RL then follows the standard hyperbolic activation curve $f(L)\equiv\frac{RL}{RL+R}=\frac{L}{K+L}$ shown in Fig. 2*B*, where R and RL denote the number of inactive and active receptor complexes, respectively. Varying the dissociation constant K simply shifts the curve in log-concentration space (44) (*SI Appendix*, section 3), so that weakly binding ligand can always saturate the receptors when $L\gg K$. This feature persists when lateral allostery between subunits makes binding cooperative (45, 46); we therefore do not consider cooperativity below.

Second, a large class of receptors including the type I and type II cytokine receptor families are activated via ligand-induced oligomerization (47). Here, ligand binding induces cross-linking of receptor subunits in the membrane, followed by cytosolic receptor cross-activation and downstream signaling (48). Although it can occur in conjunction with allosteric transmission (49–54), in the following we consider pure oligomerization for clarity. The simplest variant is homodimerization as depicted in Fig. 2*C*, where a symmetric bivalent ligand first binds from bulk solution, $\mathrm{R}+\mathrm{L}\rightleftharpoons\mathrm{RL}$ with dissociation constant K^B, and then receptors cross-link in the membrane via the ligand, $\mathrm{RL}+\mathrm{R}\rightleftharpoons\mathrm{RLR}=\mathrm{C}$ with dissociation constant K^X. For a given total number of receptor monomers $2R_0=2C+R+RL$, the equilibrium fraction of activated receptors $f=C/R_0$ is obtained as follows (23, 44, 55, 56) (*SI Appendix*, section 3):

$$f(L)=F(\Delta)\equiv 1-\left(\sqrt{\Delta^2+2\Delta}-\Delta\right);\ \Delta=\frac{K^X}{2R_0}\frac{(2L+K^B)^2}{4LK^B}, \quad [7]$$

where the auxiliary function F decreases from 1 to 0. The activation curves Eq. **7** are bell-shaped and symmetric on a log-ligand concentration scale as shown in Fig. 2*D*. After reaching a peak,

$$f_{\max}=f(K^B/2)=F(K^X/R_0), \quad [8]$$

activation decreases at high ligand concentrations as scarce free R prevent ternary complex formation (57). Because $f_{\max}$ decreases with increasing K^X, weakly cross-linking ligands fail to fully activate the receptor at any concentration (49, 58), suggesting that homodimerizing systems could improve ligand discrimination over allosteric transmission. Fig. 2*D* also shows that the curves form a one-parameter family with deactivation point approaching $L_{\mathrm{deact}}=R_0/(2\lambda)$. This feature is a consequence of the assumption that all ligand–receptor complexes share a common binding mode (49), which implies that the binding length scale $\lambda=K^X/K^B=const.$ is independent of ligand affinity (*SI Appendix*, section 3). Indeed, IFNAR–IFN cocomplex structures are structurally similar (17, 58), and we find $\lambda\simeq 5$ nm across IFNα variants with a range of affinities (59–62) (*SI Appendix*, Table S1). We impose a fixed receptor density $R_0=1\ \mu\mathrm{m}^{-2}$ (17) throughout, which gives a limiting half-deactivation point $L_{\mathrm{deact}}=166$ nM. Within the family high peak activation $f_{\max}$ requires early activation, which suggests that simultaneous sensing of ligand presence and type may be limited.

Finally, type I, type II, and immunoglobulin-like cytokine receptors comprise multiple chains that bind ligand with different affinities (see, e.g., ref. 57). In particular, the ligand affinity of IFNAR2 is about 1,000-fold higher than that of IFNAR1 (41, 58). As depicted in Fig. 2*E*, we therefore consider a ligand with two distinct binding sites, each of which binds a cognate receptor chain, $\mathrm{R}_i+\mathrm{L}\rightleftharpoons\mathrm{R}_i\mathrm{L}$ for $i=1,2$. The active complex $\mathrm{C}=\mathrm{R}_1\mathrm{LR}_2$ is then formed by cross-linking $\mathrm{R}_1+\mathrm{R}_2\mathrm{L}\rightleftharpoons\mathrm{C}$ and vice versa. There are now four dissociation constants, K_i^B, K_i^X. For 1:1

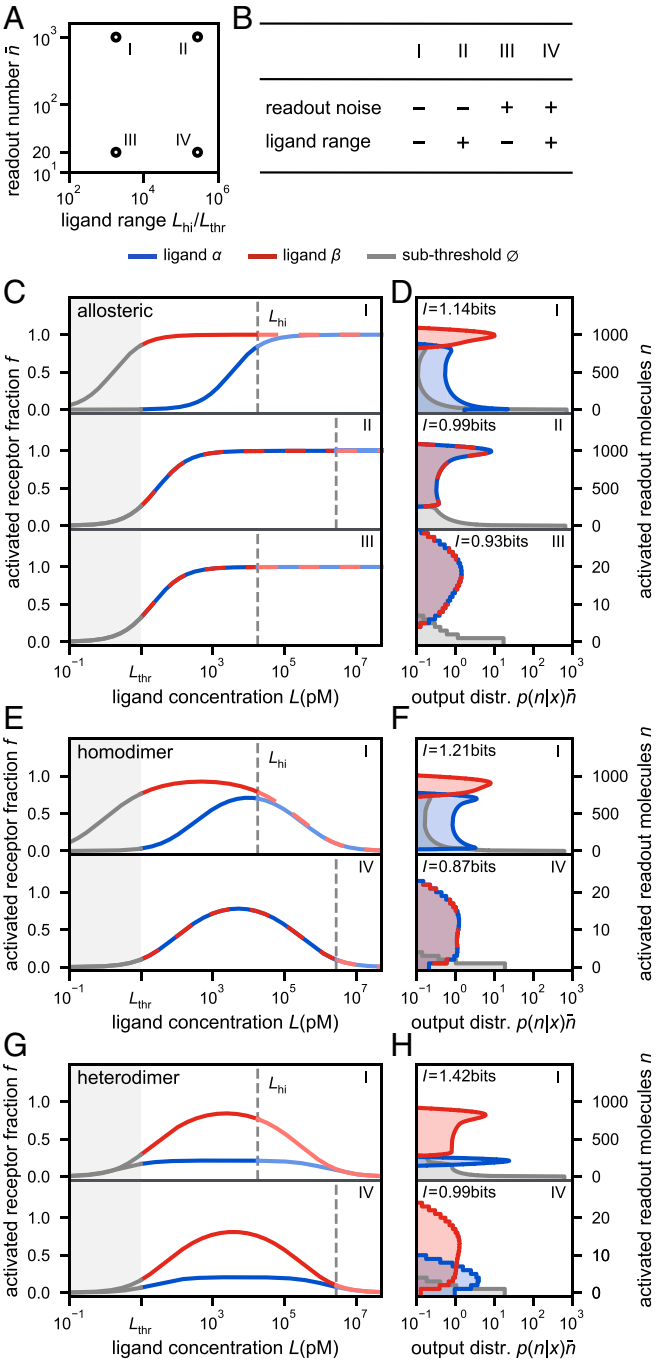

Fig. 3. Optimal ligand discrimination in basic receptor architectures. (*A*) Parameter space of readout noise and ligand concentration fluctuations with parameter points for example cases I–IV. (*B*) Definition of four paradigmatic test cases. (*C*) Optimal activation curves for allosteric receptors. Ligands are separated in case I but equal affinities for ligands are optimal in cases II and III. (*D*) Readout distributions corresponding to *B*. Case I, ligands α and β are separated but α overlaps with no ligand ($\varnothing$). II and III, ligands α and β superimpose (dashed curves) but are separated from $\varnothing$, indicating pure presence sensing. (*E*) Optimal activation curves for homodimerizing receptors. (*F*) Readout distributions corresponding to *D*. Case I, α and β are separated, but α overlaps with $\varnothing$. IV, pure presence sensing. (*G*) Optimal activation curves for heterodimerizing receptors. (*H*) Readout distributions corresponding to *F*. Case I, α, β, and $\varnothing$ are well separated. IV, all distributions are distinct but still overlap somewhat due to readout noise and deactivation at high concentration. Optimal parameter values are detailed in *SI Appendix*, Table S5.

stoichiometry of receptor chains (17), i.e., $R_i + R_i L + C = R_0$, one obtains the activated fraction $f = C/R_0$ as follows (63) (*SI Appendix*, section 3):

$$f(L) = F(\tilde{\Delta}), \text{ where } \tilde{\Delta} = \frac{K_1^X}{R_0}\frac{(L+K_1^B)(L+K_2^B)}{2LK_1^B}. \quad [9]$$

Detailed balance requires $K_1^X/K_1^B = K_2^X/K_2^B = \lambda$, so that the activation curves are controlled by the two parameters K_1^B and K_2^B. As shown in Fig. 2*F*, they are symmetric in log-concentration about a maximum:

$$f_{\max} = f\left(\sqrt{K_1^B K_2^B}\right) = F\left(\frac{1}{2}\left[\sqrt{K_1^X/R_0} + \sqrt{K_2^X/R_0}\right]^2\right), \quad [10]$$

which shows that to obtain full activation, both affinities have to be high. The activation curves show pronounced plateaus at tunable activation, which suggests they may help discrimination by concentration buffering. Half-deactivation is unchanged at L_{deact}, consistent with the IFN system (61).

Robust Ligand Discrimination Requires Asymmetric Dimerization of Receptors. We are now in a position to calculate the central quantity of our theory, namely, the mutual information or discrimination power I as defined in Eq. **1**. To compare the performance achievable with each of the three architectures, in each case we optimize I with respect to the model parameters. We consider conditions of increasing difficulty, by varying the range of concentration fluctuations $L_{\text{hi}}/L_{\text{thr}}$ from 10^2- to 10^6-fold and the readout number $\bar{n}$ from 1,500 to 10, see Fig. 3*A*. We highlight four paradigmatic cases labeled I–IV as detailed in Fig. 3*B*. Case I is a relatively easy task as it has low readout noise and a narrow ligand range. In cases II and III, ligand range and readout noise are increased, respectively. Case IV is the most challenging, with high readout noise and a broad ligand range.

We start again with allosteric transmission (cf. Fig. 2 *A* and *B*) and optimize I with respect to the dissociation constants for the two ligands: $I_{\max} = \max_{K_\alpha, K_\beta} I[p(n,x)]$. The results are shown in Fig. 3 *C* and *D*. For the easy case I, optimal discrimination results by setting the activation points K_β and K_α somewhat below the lower and upper boundaries of the ligand concentration range (Fig. 3*C*, case I, red and blue curves, respectively). Just separating the output distributions $p(n|\alpha)$ and $p(n|\beta)$ (blue and red curves) would be better achieved by choosing K_β as low and K_α as high as possible within the optimization range; this would maximize $I_\tau \to 1.0$ bit. However, because Eq. **3** incorporates presence sensing as part of the receptor performance, for optimal I also subthreshold ligand $p(n|\varnothing)$ (gray curve) needs to be distinguished. The best compromise results by allowing more overlap between ligand α and no ligand, giving $I_\pi = 0.66$ bits, and less overlap between the ligands, $I_\tau = 0.97$ bits, yielding $I_{\max} = 1.14$ bits overall. Increasing L_{hi} worsens the overlap of $p(n|\alpha)$ and $p(n|\varnothing)$, reducing I_π. Eventually, the strategy of separating $p(n|\alpha)$ and $p(n|\beta)$ is overtaken by one of equal affinities $K_\alpha = K_\beta$ (Fig. 3 *C* and *D*, case II). Only ligand presence is detected; type information is disregarded entirely ($I_\tau = 0$ bits), which limits the performance to $I_{\max} < 1$ bit. When decreasing the readout number $\bar{n}$, the readout distributions become noisier (Fig. 3 *C* and *D*, case III). This creates a tiling problem: Separating $p(n|\alpha)$ and $p(n|\beta)$ necessarily increases the overlap of $p(n|\alpha)$ and $p(n|\varnothing)$. Optimal ligand discrimination is again achieved by equal affinities for both ligands.

To assess discrimination power of homodimerizing receptors, we optimize I with respect to K_α^B and K_β^B (cf. Fig. 2 *C* and *D* and Eq. **7**). As for allosteric receptors, for low readout noise and narrow concentration range the ligands α and β can be separated (Fig. 3 *E* and *F*, case I), but here, high type information $I_\tau = 0.97$ bits is achieved through different peak activation levels of β and α. Presence information $I_\pi = 0.73$ bits is limited by the early activation of ligand β required for a high peak. When L_{hi} is increased beyond the deactivation point L_{deact}, high concentrations of either ligand can deactivate the receptors. The resulting additional overlap of readout distributions impedes accurate type sensing. Increasing also the noise level aggravates the tiling problem. Performance degrades severely, and type sensing is completely abandoned (Fig. 3*E*, case IV).

Finally, to assess the improvement in discrimination afforded by activation plateaus in heterodimerizing receptors, we optimize the discrimination power I with respect to $K_{1,\alpha}^B, K_{2,\alpha}^B, K_{1,\beta}^B, K_{2,\beta}^B$ (cf. Fig. 2 *E* and *F* and Eq. **9**). As expected, in the easy case of low concentration range and low noise, the output distributions for α, β and $\varnothing$ are separated well, with $I_{\max} = 1.42$ bits resulting from perfect type sensing ($I_\tau = 1.00$ bits) and good presence sensing ($I_\pi = 0.92$ bits) (Fig. 3 *G* and *H*, case I). When challenging the system by broad concentration range and high noise, broader output distributions overlap (Fig. 3 *G* and *H*, case IV), reducing the discrimination power to $I_{\max} = 0.99$ bits.

Fig. 4 summarizes the overall discrimination power of the three considered receptor architectures. Allosteric transmission can achieve some discrimination power by prioritizing type sensing as long as the noise level is low and concentrations are well controlled (Fig. 4 *A* and *B*, *Upper Left* region). Otherwise, least information is lost by redundantly sensing ligand presence, entirely foregoing type sensing (Fig. 4 *A* and *B*, *Lower Right*). We conclude that allosteric transmission with readout of the activated fraction f cannot achieve robust ligand discrimination. Discrimination with allosteric receptors requires readout of ligand dwell-times by nonequilibrium postprocessing. Homodimerizing systems separate ligand types based on their peak

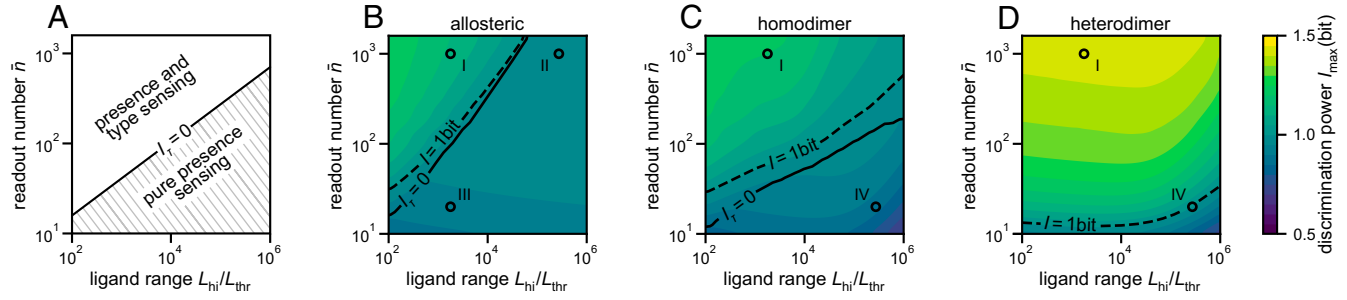

Fig. 4. Discrimination power vs. concentration range and readout number. (*A*) Pure presence sensing is optimal below the solid line $I_\tau = 0$. (*B*) Allosteric receptors achieve type sensing only in a regime of low readout noise and well-controlled concentrations (*Upper Left* corner). (*C*) Homodimerizing receptors moderately improve discrimination power and enlarge the type sensing regime. (*D*) Heterodimerizing receptors accommodate type sensing even for high noise and broad concentration ranges. Cases I–IV are as in Fig. 3.

activation levels in a slightly expanded regime of well-controlled ligand concentrations and low noise levels (Fig. 4*C*, *Upper Left*). Outside this regime, performance drops and can fall below that of allosteric receptors, mainly due to false-negative detection at high concentrations. By contrast, asymmetric binding allows type sensing even for broad concentration ranges, improving greatly on the performance of homodimerizing systems (Fig. 4*D*). Discrimination is still somewhat limited by the constraint that high activation levels require early activation, by the finite slope of the activation curves, and by possible deactivation at very high concentrations.

Receptor Turnover Adjusts Activation and Deactivation Points. We finally discuss how the nonequilibrium process of receptor turnover affects the equilibrium ligand discrimination mechanisms considered so far. For allosteric receptors, turnover simply shifts the activation point, which does not change the response repertoire and therefore neither helps nor hurts ligand discrimination (*SI Appendix*, section 4). However, turnover has a strong effect in dimerizing systems.

First, consider the homodimerizing system with turnover:

$$\mathrm{R}+\mathrm{L}\underset{k_u}{\overset{2k_b}{\rightleftharpoons}}\mathrm{RL};\quad \mathrm{RL}+\mathrm{R}\underset{2k_d}{\overset{k_a}{\rightleftharpoons}}\mathrm{C};$$
$$\mathrm{R}\underset{R_0\mu}{\overset{\mu}{\rightleftharpoons}}\varnothing;\quad \mathrm{RL}\xrightarrow{\mu}\varnothing;\quad \mathrm{C}\xrightarrow{\mu}\varnothing; \qquad [11]$$

where $k_{b,u}$ are binding and unbinding rates per binding site, $k_{a,d}$ are cross-linking association and dissociation rates per binding site, μ is the turnover rate, and the supply rate $R_0\mu$ ensures an unchanged total receptor surface density R_0 in steady state.

The nonequilibrium steady-state of Eq. **11** is controlled by the affinity K^B and two new timescales $\tau_u=\mu/k_u$ and $\tau_d=\mu/k_d$. Our analytic result for $f(L)$ (*SI Appendix*, section 4) shows that turnover shifts the limiting deactivation point $L_{\mathrm{deact}}=\frac{R_0}{2\lambda}\frac{2+3\tau_u}{2+\tau_d}$ toward higher or lower concentrations for $3k_d \gtrless k_u$, respectively, reflecting a competition of internalization of binary vs. ternary complexes. The maximal activation $f_{\max}=F([1+\tau_d/2]K^X/R_0)$ is decreased below the equilibrium value when receptor turnover is faster than dissociation (cf. Eqs. **7** and **8**).

To quantify how the larger design space affects the achievable ligand discrimination power, we optimize I with respect to K^B, k_u and k_d for ligand α and β, respectively. We fix the turnover rate $\mu=10^{-3}\mathrm{s}^{-1}$, typical for cytokine receptors (64, 65) (*SI Appendix*, section 5). Homodimerizing receptors with turnover resolve some ligand-type information even for broad ligand concentration fluctuations and high noise (Fig. 5 *A* and *B*, first row). Performance generally improves over the equilibrium homodimerizing but not the equilibrium heterodimerizing system (Fig. 5*C*; cf. Fig. 4 *C* and *D*). The improvement is mainly due to the ability of the system to align activation points of weak and strong ligands, reducing ligand presence ambiguity.

Combining turnover and asymmetric binding by repeating Eq. **11** for each R_i, one obtains an architecture that closely resembles the IFNAR system. The response curves are now controlled by a total of six parameters: $K_i^B, \tau_{u,i}, \tau_{d,i}$ defined as above, for each receptor chain $i=1,2$. The optimized activation curves now exhibit broad plateaus at both high and low activation levels, activation points aligned at the threshold L_{thr}, and deactivation points beyond $L_{\max}$ (Fig. 5*A*, second row). This effectively reduces output overlap between α and β (Fig. 5*B*) by buffering concentration fluctuations ($I_\tau=0.83$ bits, $I_\pi=0.79$ bits, $I=1.21$ bits), approaching the performance of the theoretically ideal step-like response functions (Fig. 5 *A* and *B*, third row). The performance becomes essentially independent of concentration fluctuations (Fig. 5*D*).

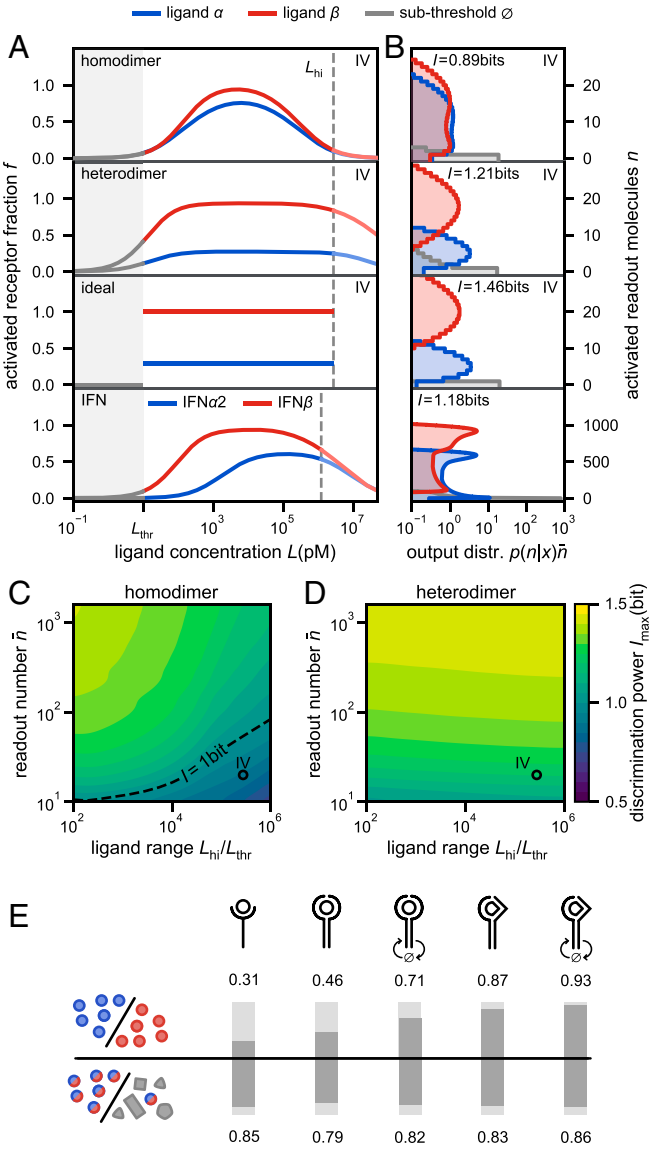

Fig. 5. Ligand discrimination by dimerizing receptors including receptor turnover. (*A*) Optimal activation curves. From *Top* to *Bottom*: homodimer case IV; heterodimerizing case IV; ideal step response case IV; IFN: activation curves of IFNα2 and IFNβ at lower readout noise. (*B*) Corresponding readout distributions. Homodimer, poor separation of α and β; heterodimer and ideal, excellent separation of α, β and $\varnothing$; IFN, good separation at lower noise. Optimal parameter values are detailed in *SI Appendix*, Table S5. (*C* and *D*) Optimal discrimination power vs. concentration range and readout number (cf. Fig. 4 *C* and *D*). Turnover improves performance in the well-controlled regime for homodimers (*C*), and in all conditions for heterodimers (*D*). (*E*) Overall discrimination power of all considered receptor architectures. Type information I_τ (upper row) and presence information I_π (lower row) averaged over the parameter range shown in *C* and *D* are indicated as a fraction of the maximum 1 bit.

Does IFNAR actually exploit the possibilities of its architecture for ligand discrimination? Literature values of IFNAR kinetic rates show that IFNs bind chain IFNAR2 with much higher affinity than IFNAR1, and IFNβ binds both with higher affinity than IFNα2 (*SI Appendix*, Table S6). This ordering agrees with that of our optimal rates for heterodimerizing receptors with turnover (*SI Appendix*, Table S5). Fig. 5 *A* and *B*, last row, shows activation curves corresponding to the literature rate values, where optimization was carried out with respect to the receptor density R_0 and the upper cutoff L_{hi}. Although they

lack alignment of the activation points, these unmodified activation curves are similar in shape to our optimal solutions. The performance is remarkable at $I_{\max} = 1.18$ bits.

Discussion

Cell-to-cell communication in tissues is challenged by highly variable local cytokine concentrations at receiving cells. This fundamental uncertainty can be circumvented by encoding the signal digitally in the chemical properties of cytokines rather than proportionally in cytokine concentration. Reliable communication then rests on the cells' ability to discriminate between different ligands in presence of large concentration fluctuations.

Using information theory, here we have quantified how well receptors discriminate ligands at the membrane. Ligand presence sensing and type sensing are necessary ingredients for functional ligand discrimination; while all architectures can sense ligand presence well (Fig. 5*E*), we find that readout of bound fractions of allosteric receptors cannot achieve robust type sensing. Receptor dimerization offers only a partial solution (23) as concentration fluctuations confound ligand type. Robust type sensing is achieved only by strongly asymmetric binding of ligand to the two receptor chains, rendering receptor activation both ligand type dependent and concentration independent. When receptor turnover drives the system out of equilibrium, the activation curves can come close to a theoretically perfect discriminator. The fact that actual biochemical parameters realized by IFNAR come close to this ideal supports the hypothesis that ligand discrimination is at the core of the biological function of this system (17). Our results further suggest that ligand-discriminating receptors should favor an asymmetrically dimerizing architecture, while single-ligand receptors have no need for asymmetry. In accordance with this prediction, type I and type III IFN receptors feature multiple ligands and asymmetry, whereas type II receptors bind only IFNγ and activate by homodimerization (66).

Here, we have considered noise arising by readout activation (Eq. **5**), but also ligand–receptor binding from cell-to-cell variability in receptor and readout molecule numbers will degrade the signal. We found that when considering only constitutive genes, the effect of these additional noise sources can be approximated well by an effective readout number $\bar{n}$. In particular, *SI Appendix*, Fig. S3 shows that typical protein number fluctuations of about 25% have an effect similar to reducing $\bar{n}$ from 100 to 20.

To arrive at definite results, here we have assumed equal chances for ligand being absent or present, and of either type. Alternatively, one could argue that ligands should be present only in rare situations of acute inflammation, or that the more potent ligand may occur more rarely than the other. Rare presence of ligands reduces the contribution from type sensing to Eq. **3**, while unequal ligand frequencies reduce the total information encoded in ligand type. To investigate the implications, we have reoptimized the discrimination power for these alternative scenarios (*SI Appendix*, Fig. S4). Both modifications cause presence sensing to be preferred over a wider range, but heterodimerizing receptors can still accommodate type sensing; the corresponding optimal response functions remain essentially unchanged. Thus, a balance of presence and type sensing emerges as a generic feature of ligand discrimination. Our theory may be further refined to account for the relative value of certain bits of information compared to others; for instance, some rarely occurring ligands may nevertheless be essential for survival. Assignment of fitness values to certain ligands using the tools of decision theory remains an interesting open question.

Ligand-induced oligomerization may occur in combination with other mechanisms for ligand discrimination. Nonequilibrium dwell-time sensing via modified kinetic proofreading schemes is known to mediate ligand specificity in T cells (28, 32) and could contribute to sensing also in dimerizing systems via nonequilibrium receptor phosphorylation kinetics. Dynamical features of the downstream response such as slow negative feedback via USP18 (17, 18) may further improve ligand discrimination. Finally, in a tissue context, ligands are unlikely to always occur one type at a time. The interaction of multiple ligands at once leads to combinatorial responses including antagonism (31) and signal integration (67). In particular, ratiometric responses are unaffected by concentration fluctuations and thus may provide cells with a robust parallelized digital signaling channel. We expect that information-theoretic methods as used here will prove useful in elucidating the specific advantages of membrane receptor architectures and, eventually, full pathways.

Methods

We estimated the maximal discrimination power Eq. **1** achievable by each considered receptor architecture using Dual Annealing (68) as implemented in Scipy 1.5.0 (69). Parameter ranges for dissociation constants and on-rates and fixed values for receptor density, activation threshold, and diffusivity were fixed based on typical ranges in the IFN system and biophysical constraints (17, 41, 44, 59–62, 64, 65). For further details, see *SI Appendix*, section 5.

Data Availability. All study data are included in the article and/or supporting information.

ACKNOWLEDGMENTS. P.B. was supported by the Research Training Group on Mathematical Modeling for the Quantitative Biosciences at Heidelberg. T.H. and U.S.S. acknowledge support as members of the Collaborative Research Center 1129 of the German Research Foundation funded under Projektnummer 240245660.

1. J. J. Tyson, K. C. Chen, B. Novak, Sniffers, buzzers, toggles and blinkers: Dynamics of regulatory and signaling pathways in the cell. *Curr. Opin. Cell Biol.* **15**, 221–231 (2003).
2. R. Cheong, A. Rhee, C. J. Wang, I. Nemenman, A. Levchenko, Information transduction capacity of noisy biochemical signaling networks. *Science* **334**, 354–358 (2011).
3. J. Selimkhanov *et al*., Systems biology. Accurate information transmission through dynamic biochemical signaling networks. *Science* **346**, 1370–1373 (2014).
4. T. M. Cover, J. A. Thomas, *Elements of Information Theory* (Wiley, 2012).
5. C. C. Govern, P. R. Ten Wolde, Optimal resource allocation in cellular sensing systems. *Proc. Natl. Acad. Sci. U.S.A.* **111**, 17486–17491 (2014).
6. P. R. ten Wolde, N. B. Becker, T. E. Ouldridge, A. Mugler, Fundamental limits to cellular sensing. *J. Stat. Phys.* **162**, 1395–1424 (2016).
7. S. Takahashi, P. M. Pryciak, Membrane localization of scaffold proteins promotes graded signaling in the yeast MAP kinase cascade. *Curr. Biol.* **18**, 1184–1191 (2008).
8. M. Hinczewski, D. Thirumalai, Cellular signaling networks function as generalized Wiener-Kolmogorov filters to suppress noise. *Phys. Rev. X* **4**, 1–15 (2014).
9. H. E. Grecco, M. Schmick, P. I. H. Bastiaens, Signaling from the living plasma membrane. *Cell* **144**, 897–909 (2011).
10. N. B. Becker, A. Mugler, P. R. Ten Wolde, Optimal prediction by cellular signaling networks. *Phys. Rev. Lett.* **115**, 258103 (2015).
11. A. Mugler, A. G. Bailey, K. Takahashi, P. R. ten Wolde, Membrane clustering and the role of rebinding in biochemical signaling. *Biophys. J.* **102**, 1069–1078 (2012).
12. A. Mugler, F. Tostevin, P. R. ten Wolde, Spatial partitioning improves the reliability of biochemical signaling. *Proc. Natl. Acad. Sci. U.S.A.* **110**, 5927–5932 (2013).
13. P. B. Detwiler, S. Ramanathan, A. Sengupta, B. I. Shraiman, Engineering aspects of enzymatic signal transduction: Photoreceptors in the retina. *Biophys. J.* **79**, 2801–2817 (2000).
14. B. M. C. Martins, P. S. Swain, Trade-offs and constraints in allosteric sensing. *PLoS Comput. Biol.* **7**, e1002261 (2011).
15. A. Levchenko, I. Nemenman, Cellular noise and information transmission. *Curr. Opin. Biotechnol.* **28**, 156–164 (2014).
16. T. Maiwald *et al*., Combining theoretical analysis and experimental data generation reveals IRF9 as a crucial factor for accelerating interferon α-induced early antiviral signalling. *FEBS J.* **277**, 4741–4754 (2010).
17. J. Piehler, C. Thomas, K. C. Garcia, G. Schreiber, Structural and dynamic determinants of type I interferon receptor assembly and their functional interpretation. *Immunol. Rev.* **250**, 317–334 (2012).
18. G. Schreiber, J. Piehler, The molecular basis for functional plasticity in type I interferon signaling. *Trends Immunol.* **36**, 139–149 (2015).
19. W. de Ronde, F. Tostevin, P. R. ten Wolde, Multiplexing biochemical signals. *Phys. Rev. Lett.* **107**, 048101 (2011).

20. D. Levin *et al*., Multifaceted activities of type I interferon are revealed by a receptor antagonist. *Sci. Signal.* **7**, ra50 (2014).
21. I. Otero-Muras, P. Yordanov, J. Stelling, Chemical reaction network theory elucidates sources of multistability in interferon signaling. *PLoS Comput. Biol.* **13**, e1005454 (2017).
22. C. You *et al*., Receptor dimer stabilization by hierarchical plasma membrane microcompartments regulates cytokine signaling. *Sci. Adv.* **2**, e1600452 (2016).
23. S. Fathi, C. R. Nayak, J. J. Feld, A. G. Zilman, Absolute ligand discrimination by dimeric signaling receptors. *Biophys. J.* **111**, 917–920 (2016).
24. T. W. McKeithan, Kinetic proofreading in T-cell receptor signal transduction. *Proc. Natl. Acad. Sci. U.S.A.* **92**, 5042–5046 (1995).
25. G. Altan-Bonnet, R. N. Germain, T. Modeling, Modeling T cell antigen discrimination based on feedback control of digital ERK responses. *PLoS Biol.* **3**, e356 (2005).
26. P. François, G. Voisinne, E. D. Siggia, G. Altan-Bonnet, M. Vergassola, Phenotypic model for early T-cell activation displaying sensitivity, specificity, and antagonism. *Proc. Natl. Acad. Sci. U.S.A.* **110**, E888–E897 (2013).
27. P. François, G. Altan-Bonnet, The case for absolute ligand discrimination: Modeling information processing and decision by immune T cells. *J. Stat. Phys.* **162**, 1130–1152 (2016).
28. P. François, A. Zilman, Physical approaches to receptor sensing and ligand discrimination. *Curr. Opin. Syst. Biol.* **18**, 111–121 (2019).
29. T. Mora, Physical limit to concentration sensing amid spurious ligands. *Phys. Rev. Lett.* **115**, 038102 (2015).
30. V. Singh, I. Nemenman, Simple biochemical networks allow accurate sensing of multiple ligands with a single receptor. *PLoS Comput. Biol.* **13**, e1005490 (2017).
31. J. B. Lalanne, P. François, Chemodetection in fluctuating environments: Receptor coupling, buffering, and antagonism. *Proc. Natl. Acad. Sci. U.S.A.* **112**, 1898–1903 (2015).
32. O. S. Yousefi *et al*., Optogenetic control shows that kinetic proofreading regulates the activity of the T cell receptor. *eLife* **8**, e42475 (2019).
33. G. Altan-Bonnet, T. Mora, A. M. Walczak, Quantitative immunology for physicists. *Phys. Rep.* **849**, 1–83 (2020).
34. A. Rhee, R. Cheong, A. Levchenko, The application of information theory to biochemical signaling systems. *Phys. Biol.* **9**, 045011 (2012).
35. A. M. Walczak, G. Tkačik, Information transmission in genetic regulatory networks: A review. *J. Phys. Condens. Matter* **23**, 153102 (2011).
36. C. G. Bowsher, M. Voliotis, P. S. Swain, The fidelity of dynamic signaling by noisy biomolecular networks. *PLoS Comput. Biol.* **9**, e1002965 (2013).
37. A. Oyler-Yaniv *et al*., A tunable diffusion-consumption mechanism of cytokine propagation enables plasticity in cell-to-cell communication in the immune system. *Immunity* **46**, 609–620 (2017).
38. A. J. Müller *et al*., $CD4^+$ T cells rely on a cytokine gradient to control intracellular pathogens beyond sites of antigen presentation. *Immunity* **37**, 147–157 (2012).
39. G. Altan-Bonnet, R. Mukherjee, Cytokine-mediated communication: A quantitative appraisal of immune complexity. *Nat. Rev. Immunol.* **19**, 205–217 (2019).
40. E. T. Jaynes, "Prior probabilities" in *IEEE Transactions on Systems Science and Cybernetics* (IEEE, 1968), vol. 4, pp. 227–241.
41. T. B. Lavoie *et al*., Binding and activity of all human alpha interferon subtypes. *Cytokine* **56**, 282–289 (2011).
42. F. Trettel *et al*., Ligand-independent CXCR2 dimerization. *J. Biol. Chem.* **278**, 40980–40988 (2003).
43. S. J. Allen, S. E. Crown, T. M. Handel, Chemokine: Receptor structure, interactions, and antagonism. *Annu. Rev. Immunol.* **25**, 787–820 (2007).
44. D. A. Lauffenburger, J. J. Linderman, *Receptors: Models for Binding, Trafficking, and Signaling* (Oxford University Press, New York, 1993).
45. J Monod, J Wyman, J Changeux, On nature of allosteric transitions—a plausible model. *J. Mol. Biol.* **12**, 88 (1965).
46. D. Bray, T. Duke, Conformational spread: The propagation of allosteric states in large multiprotein complexes. *Annu. Rev. Biophys. Biomol. Struct.* **33**, 53–73 (2004).
47. C. H. Heldin, Dimerization of cell surface receptors in signal transduction. *Cell* **80**, 213–223 (1995).
48. J. T. Hancock, *Cell Signalling* (Oxford University Press, 2017).
49. A. Whitty, C. W. Borysenko, Small molecule cytokine mimetics. *Chem. Biol.* **6**, R107–R118 (1999).
50. Y. Nakamura *et al*., Heterodimerization of the IL-2 receptor β- and γ. *Nature* **369**, 330–333 (1994).
51. B. H. Nelson, J. D. Lord, P. D. Greenberg, Cytoplasmic domains of the interleukin-2 receptor β and γ chains mediate the signal for T-cell proliferation. *Nature* **369**, 333–336 (1994).
52. S. Damjanovich *et al*., Preassembly of interleukin 2 (IL-2) receptor subunits on resting Kit 225 K6 T cells and their modulation by IL-2, IL-7, and IL-15: A fluorescence resonance energy transfer study. *Proc. Natl. Acad. Sci. U.S.A.* **94**, 13134–13139 (1997).
53. J. W. Cotari, G. Voisinne, O. E. Dar, V. Karabacak, G. Altan-Bonnet, Cell-to-cell variability analysis dissects the plasticity of signaling of common γ chain cytokines in T cells. *Sci. Signal.* **6**, ra17 (2013).
54. J. Volkó *et al*., IL-2 receptors preassemble and signal in the ER/Golgi causing resistance to antiproliferative anti-IL-2Rα therapies. *Proc. Natl. Acad. Sci. U.S.A.* **116**, 21120–21130 (2019).
55. A. S. Perelson, C. DeLisi, Receptor clustering on a cell surface. I. Theory of receptor cross-linking by ligands bearing two chemically identical functional groups. *Math. Biosci.* **48**, 71–110 (1980).
56. J. Yang, W. S. Hlavacek, Scaffold-mediated nucleation of protein signaling complexes: Elementary principles. *Math. Biosci.* **232**, 164–173 (2011).
57. M. Atanasova, A. Whitty, Understanding cytokine and growth factor receptor activation mechanisms. *Crit. Rev. Biochem. Mol. Biol.* **47**, 502–530 (2012).
58. E. Jaks, M. Gavutis, G. Uzé, J. Martal, J. Piehler, Differential receptor subunit affinities of type I interferons govern differential signal activation. *J. Mol. Biol.* **366**, 525–539 (2007).
59. M. Gavutis, S. Lata, P. Lamken, P. Müller, J. Piehler, Lateral ligand-receptor interactions on membranes probed by simultaneous fluorescence-interference detection. *Biophys. J.* **88**, 4289–4302 (2005).
60. M. Gavutis, E. Jaks, P. Lamken, J. Piehler, Determination of the two-dimensional interaction rate constants of a cytokine receptor complex. *Biophys. J.* **90**, 3345–3355 (2006).
61. F. Roder, S. Wilmes, C. P. Richter, J. Piehler, Rapid transfer of transmembrane proteins for single molecule dimerization assays in polymer-supported membranes. *ACS Chem. Biol.* **9**, 2479–2484 (2014).
62. S. Wilmes *et al*., Receptor dimerization dynamics as a regulatory valve for plasticity of type I interferon signaling. *J. Cell Biol.* **209**, 579–593 (2015).
63. A. S. Perelson, Receptor clustering on a cell surface. II. Theory of receptor cross-linking by ligands bearing two chemically distinct functional groups. *Math. Biosci.* **49**, 87–110 (1980).
64. K. G. S. Kumar *et al*., Site-specific ubiquitination exposes a linear motif to promote interferon-alpha receptor endocytosis. *J. Cell Biol.* **179**, 935–950 (2007).
65. K. G. S. Kumar *et al*., Basal ubiquitin-independent internalization of interferon alpha receptor is prevented by Tyk2-mediated masking of a linear endocytic motif. *J. Biol. Chem.* **283**, 18566–18572 (2008).
66. J. L. Mendoza *et al*., Structure of the IFNγ receptor complex guides design of biased agonists. *Nature* **567**, 56–60 (2019).
67. Y. E. Antebi *et al*., Combinatorial signal perception in the BMP pathway. *Cell* **170**, 1184–1196.e24 (2017).
68. Y. Xiang, D. Y. Sun, W. Fan, X. G. Gong, Generalized simulated annealing algorithm and its application to the Thomson model. *Phys. Lett. A* **233**, 216–220 (1997).
69. P. Virtanen *et al*., SciPy 1.0: Fundamental algorithms for scientific computing in Python. *Nat. Methods* **17**, 261–272 (2020).